Mathematical modelling of fluid flow and solute transport to define operating parameters for *in vitro* perfusion cell culture systems

Lauren Hyndman[1], Sean McKee[2], Nigel Mottram[2], Bhumika Singh[3], Steven Webb[4], and Sean McGinty[1*]

[1]Division of Biomedical Engineering, University of Glasgow, Glasgow, G12 8QQ, UK.
[2]Department of Mathematics and Statistics, University of Strathclyde, Glasgow, G1 1XQ, UK.
[3]Kirkstall Ltd., 3 Aspen Way, Rotherham, S60 1FB, UK.
[4]Department of Applied Mathematics, Liverpool John Moores University, Liverpool, L3 5UA, UK.

[*]Corresponding author:
Sean McGinty
Division of Biomedical Engineering
University of Glasgow
Glasgow G12 8QQ
UK
Tel: 0141 330 8588
Email: sean.mcginty@glasgow.ac.uk

Abstract

In recent years, there has been a move away from the use of static *in vitro* 2D cell culture models for testing the chemical safety and efficacy of drugs. Such models are increasingly being replaced by more physiologically relevant cell culture systems featuring dynamic flow and/or 3D structures of cells. Whilst it is acknowledged that such systems provide a more realistic environment within which to test drugs, progress is being hindered by a lack of understanding of the physical and chemical environment that the cells are exposed to. Mathematical and computational modelling may be exploited in this regard to unravel the dependency of the cell response on spatiotemporal differences in chemical and mechanical cues, thereby assisting with the understanding and design of these systems. In this paper, we present a somewhat general mathematical modelling framework that characterises the fluid flow and solute transport in perfusion bioreactors featuring an inlet and an outlet. To demonstrate the utility of our model, we simulated the fluid dynamics and solute concentration profiles for a variety of different flow rates, inlet solute concentrations and cell types within a specific commercial bioreactor chamber. Our subsequent analysis has elucidated the basic relationship between inlet flow rate and cell surface flow speed, shear stress and solute concentrations, allowing us to derive simple but useful relationships that enable prediction of the behaviour of the system under a variety of experimental conditions, prior to experimentation. We describe how the model may used by experimentalists to define operating parameters for their particular perfusion cell culture systems and highlight some operating conditions that should be avoided. Finally, we critically comment on the limitations of mathematical and computational modelling in this field, and the challenges associated with the adoption of such methods.

Keywords

3D cell culture, bioreactor, mathematical and computational modelling, fluid dynamics, mass transport, drug testing.

1 Introduction

Drug discovery is a long and expensive process, with the development of a single drug taking many years to complete and the cost increasing significantly at each stage of testing [1, 2]. In addition, regulation states that animal usage in drug testing must be minimised or avoided [3]. Therefore, it is critical that the drug discovery process is as efficient as possible in order to develop drugs quickly whilst lowering costs and reducing the use of animals.

The first stage of drug development is to identify and optimise lead compounds to create potential drug molecules. Properties such as absorption, metabolism and toxicity are tested in preclinical studies (*in vitro* cell-based and *in vivo* animal-based experiments) before human clinical trials take place prior to marketing and approval of the drug. In order to maximise the efficiency of the screening process, drugs which are likely to fail need to be eliminated as early as possible. *In vitro* experiments conducted at the initial stages of testing are often poorly representative of the *in vivo* environment since cells are typically cultured under static conditions in a two-dimensional (2D) array, whereas in reality, cells in three-dimensional (3D) configurations are able to communicate with other cells whilst being exposed to flow. Animal studies are unethical, costly and often poorly predictive of the human response due to species differences. Thus, it is essential that new drug testing systems are developed which do not involve (or limit the use of) animals and which reflect the physiological environment so that drugs likely to fail will be eliminated earlier in the screening process [1, 2].

Mathematical modelling can be useful in the design and optimisation of novel drug testing systems. For example, prototypes of new devices can be built virtually and features such as geometry can be easily modified allowing the 'best' design to be chosen prior to fabrication of the device. Despite the fact that experiments are usually run with constant inlet solute concentrations (e.g. oxygen (O_2), drug, nutrients) and flow rates, spatial gradients and time-dependencies in solute concentrations and fluid forces (shear stress) often emerge, meaning that cells are not exposed to a homogeneous environment. Mathematical and computational modelling may be exploited in this regard to unravel the dependency of the cellular response on spatiotemporal differences in chemical and mechanical cues, thereby assisting with the understanding and design of these systems. A range of suitable operating parameters can then be established depending on the desired experimental outcome, allowing for the accurate configuration of devices with less reliance on a 'trial and error' approach.

Perfusion bioreactors are dynamic cell culture systems which have been gaining much attention in recent years. These systems allow cells to be cultured in 2D and 3D configurations whilst being exposed to flow. Improved cell viability and metabolic function has been observed under cell culture conditions provided by bioreactors: the presence of flow provides a supply of nutrients to the cells, co-culture promotes cell-cell interactions and cells cultured in 3D configurations are able to retain their physiological morphology [4].

There are a number of existing studies in the literature which use mathematical modelling to characterise certain perfusion bioreactors. For example, models of fluid flow and solute transport have been employed to optimise chamber design [5], design a gradient generator for drug toxicity testing [6], predict concentration gradients [7] and maximise mass transfer whilst controlling shear stress levels [8]. Most relevant to this study, a model was developed to optimise the design of a modular bioreactor chamber [9] and to assess if the O_2 delivery and shear stress levels would be acceptable for the culture of hepatocytes within a hydrogel layer [10]. More recently, models were developed to predict flow patterns, O_2 transport and test compound distribution within three different bioreactors to identify which of the systems would be most suitable for long-term culture of hepatocytes within alginate beads [11].

A key limitation of these existing models is that they account for *very specific* experiments and cell types (e.g. culturing hepatocytes within a hydrogel layer or alginate beads). Since perfusion bioreactors are increasingly being used for a variety of applications incorporating different cell types and solutes with different mechanisms of action, it is important to consider potential differences in the environment and operating conditions. In this paper, we present a more general modelling framework that characterises the fluid flow and solute transport in perfusion bioreactors featuring an inlet and an outlet. We start by presenting the model equations, initial and boundary conditions that describe the environment within an arbitrary bioreactor chamber. We consider two common types of solute reaction with the cells - nonlinear saturable binding and Michaelis-Menten (M-M) kinetics - and we use mathematical arguments to justify simplifications of the underlying equations in certain cases. We then provide simple relationships which allow for the rapid prediction of cell surface solute concentration profiles in single and connected chambers, prior to experimentation. To demonstrate the utility of our model, we simulate the fluid dynamics and solute concentration profiles for a variety of input flow rates, inlet concentrations and cell types within a specific bioreactor chamber: the Kirkstall QV900. For single and connected chambers, we examine the relationships between input flow rate and cell surface flow speeds, shear stress levels and solute concentrations and investigate the effect of varying cell-specific parameters on solute concentration profiles at the cell surface. Finally, we critically comment on the limitations of mathematical and computational modelling in this field, and the challenges associated with the adoption of such methods.

2 Mathematical and computational methods

We begin by considering an arbitrary geometry to represent a sealed bioreactor chamber featuring an inlet, an outlet and assuming that cells are cultured at the base of the chamber, either in a 3D region or within a monolayer. We note that the model is applicable to any chamber geometry with these properties. Fig. 1 illustrates how we set up the model equations to describe fluid flow and solute transport and this will be discussed in detail in the following text.

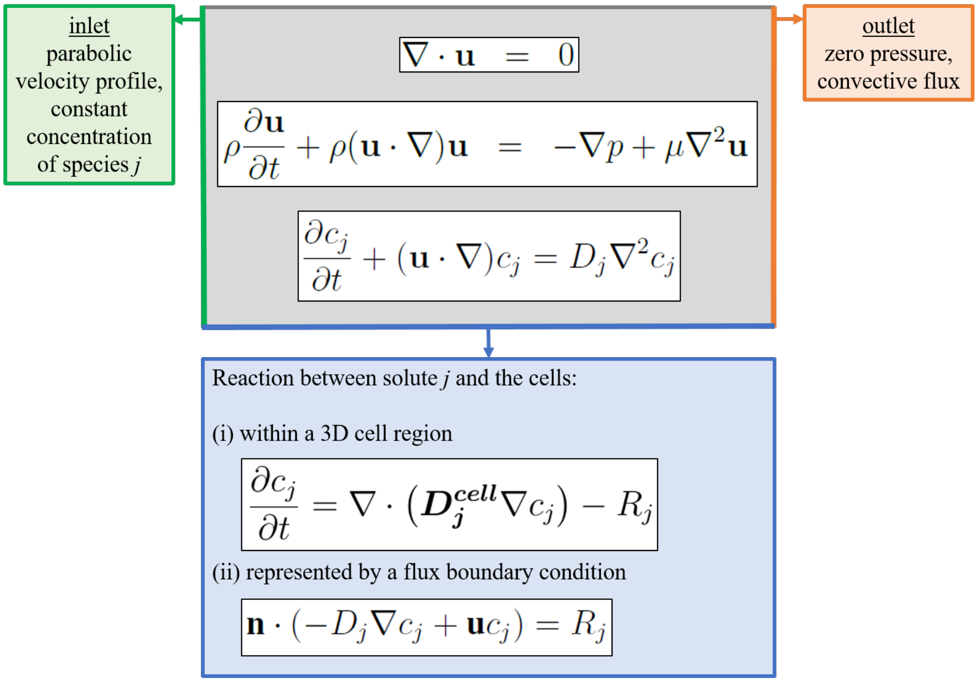

Figure 1: Schematic drawing of an arbitrary bioreactor geometry featuring an inlet and an outlet with cells cultured at the base of the chamber to illustrate the model set-up. For full details of the equations, the reader is referred to the text.

2.1 Fluid dynamics in the chamber

Assuming we have an incompressible Newtonian fluid, the flow velocity and pressure are described using the continuity and Navier-Stokes equations:

$$\nabla \cdot \mathbf{u} = 0, \tag{1}$$

$$\rho \frac{\partial \mathbf{u}}{\partial t} + \rho(\mathbf{u} \cdot \nabla)\mathbf{u} = -\nabla p + \mu \nabla^2 \mathbf{u}, \tag{2}$$

where $\mathbf{u}$ ($\mathrm{m\ s^{-1}}$) is the velocity field, p (Pa) is the pressure, ρ is the fluid density and μ is the dynamic viscosity. Initially, the fluid velocity is zero ($\mathbf{u} = \mathbf{0}$) in the chamber. At the inlet, we assume a parabolic velocity profile with magnitude derived from the volumetric flow rate, Q, which can be controlled in experiments (see Supplementary Material). We assume zero pressure ($p = 0$) at the outlet and no slip and no penetration conditions ($\mathbf{u} = \mathbf{0}$) are imposed on all interior walls.

2.2 Solute transport in the chamber

The transport of each solute through the fluid is described using a convection-diffusion equation:

$$\frac{\partial c_j}{\partial t} + (\mathbf{u} \cdot \nabla)c_j = D_j \nabla^2 c_j, \tag{3}$$

where c_j ($\mathrm{mol\ m^{-3}}$) is the concentration of solute j and D_j is the diffusion coefficient associated with solute j. We assume that each solute is present at a sufficiently low concentration such that the presence of one solute has no impact on the transport of another (*dilute assumption*). We further assume no binding of solute j to components of the fluid (e.g. proteins) but note that D_j may be adjusted to account for this process [12]. Initially, the solute concentration is zero ($c_j = 0$) in the chamber. A constant supply of each solute ($c_j = c_j^{in}$) is prescribed at the inlet and a convective flux ($-\mathbf{n} \cdot D_j \nabla c_j = 0$, where $\mathbf{n}$ is an outward facing normal) is imposed at the outlet. We assume the walls of the chamber are impermeable and impose a zero flux condition of the form $\mathbf{n} \cdot (-D_j \nabla c_j + \mathbf{u} c_j) = 0$ on all interior walls.

2.3 Solute reaction with the cells

We assume the cells are cultured at the base of the chamber either (i) within a 3D region of thickness h_c or (ii) as a monolayer. To demonstrate how we may characterise different *types* of reaction between the solute and the cells, we then present two common reaction mechanisms. First, we consider a reaction governed by nonlinear saturable binding kinetics. Then, we consider a reaction governed by Michaelis-Menten (M-M) kinetics.

2.3.1 Reaction within a 3D cell region

Within the 3D cell region, we assume no appreciable flow and so we describe solute transport using a reaction-diffusion equation:

$$\frac{\partial c_j}{\partial t} = \nabla \cdot \left(\boldsymbol{D_j^{cell}} \nabla c_j \right) - R_j^{3D}, \tag{4}$$

where $\boldsymbol{D_j^{cell}}$, the diffusivity tensor associated with solute j, is assumed to capture any heterogeneity in the cell population and, here, R_j^{3D} ($\mathrm{mol\ m^{-3}\ s^{-1}}$) describes the bulk reaction between solute j and the cells. Initially, the solute concentration is zero ($c_j = 0$) in the cell region and we assume continuity of concentration and flux across the boundary.

2.3.2 Reaction within a monolayer

If we are interested in estimating only *cell surface* solute concentration profiles of a monolayer, we may replace the 3D cell region with a flux boundary condition of the following form:

$$\mathbf{n} \cdot (-D_j \nabla c_j + \mathbf{u} c_j) = R_j^{2D}, \tag{5}$$

where, here, R_j^{2D} ($\mathrm{mol\ m^{-2}\ s^{-1}}$) describes the surface reaction between solute j and the cells. We note that (5) may also be used if we are interested in estimating solute concentrations on the surface of a 3D region of cells (as in Section 2.3.1) in the special case of homogeneous transport properties (i.e. isotropic diffusion) with the cell region.

2.3.3 Reaction governed by nonlinear saturable binding kinetics

We describe the first type of reaction by nonlinear saturable binding:

$$R_j^{3D} = k_j^f c_j (B_j - b_j) - k_j^r b_j, \tag{6}$$

where c_j $(\mathrm{mol\ m^{-3}})$ is the concentration of free drug, B_j is the local density of binding sites and k_j^f and k_j^r are the forward and reverse reaction rates, respectively. Here, we require an additional equation to track the concentration of bound drug, b_j $(\mathrm{mol\ m^{-3}})$, in the 3D cell region:

$$\frac{\partial b_j}{\partial t} = k_j^f c_j (B_j - b_j) - k_j^r b_j. \tag{7}$$

We remark that nonlinear saturable irreversible binding and linear binding kinetics may be recovered as special cases of (7) through appropriate choice of the model parameters. We also note that although we have chosen to model the binding process within a 3D cell region, these equations may be easily adapted to describe the binding process via a flux boundary condition, as in (5), by defining b_j in units of $\mathrm{mol\ m^{-2}}$ and employing an appropriate mass conservation condition.

2.3.4 Reaction governed by Michaelis-Menten kinetics

We describe the second type of solute reaction by M-M kinetics, commonly used in the literature to describe $\mathrm{O_2}$ consumption [5, 7–11] and paracetamol (APAP) metabolism [13, 14]. These kinetics describe the relationship between the concentration of solute and speed of a reaction: as solute concentration increases, the reaction rate increases before approaching a maximum for higher solute concentrations [15, 16]. In this case, we have chosen to model the metabolic process using a flux boundary condition but, again, these equations may be easily adapted to describe the metabolic process within a 3D cell region by suitably adjusting the units of the model parameters. A general M-M reaction term has the following form:

$$R_j^{2D} = \sum_{i=1}^{m} \frac{V_j^i c_j}{K_j^i + c_j}, \tag{8}$$

where m is the number of metabolic pathways involved in the reaction, K_j^i is the M-M constant for solute j and pathway i and V_j^i is the maximum reaction rate for solute j and pathway i. It may be readily shown that:

$$R_j^{2D} \approx \begin{cases} \displaystyle\sum_{i=1}^{m} V_j^i \quad \text{when} \quad \frac{K_j^i}{c_j} \ll 1 \\ \displaystyle\sum_{i=1}^{m} \frac{V_j^i c_j}{K_j^i}, \quad \text{when} \quad \frac{K_j^i}{c_j} \gg 1 \end{cases}, \tag{9}$$

so that when the ratio of K_j^i to c_j satisfies the above criteria, we can reasonably replace the full M-M kinetics (8) by the approximate expressions (9).

2.4 Derivation of relationships to inform experimental operating conditions

For each type of reaction mechanism we provide simple relationships which allow for the rapid prediction of steady-state solute concentrations, prior to experimentation.

2.4.1 Predicting steady-state solute concentrations when reaction is governed by nonlinear saturable binding kinetics

It may readily be shown (see Supplementary Material) that in the case of isotropic diffusion, we are able to reduce the nonlinear saturable binding model in the limit of rapid binding by combining (4) and (7) to obtain

$$\frac{\partial T_j}{\partial t} = \nabla \cdot (D_j^* \nabla T_j), \quad D_j^* \approx \frac{D_j^{cell}}{1 + \frac{Bk_d}{(k_d + c_j)^2}}, \tag{10}$$

where $T_j = c_j + b_j$ is the total drug concentration, D_j^* is the effective diffusion coefficient and $k_j^d = k_j^r / k_j^f$ is the equilibrium dissociation constant. It is clear that the role of binding is accounted for through a reduced diffusion coefficient. From (7) it follows that at steady-state we have:

$$b_j = \frac{Bc_j}{k_d + c_j}. \tag{11}$$

Substituting this expression into $T_j = c_j + b_j$ yields a quadratic equation in c_j which we solve to obtain:

$$c_j = -\frac{1}{2}(k_j^d + B_j - T_j) \pm \frac{1}{2}\sqrt{(k_j^d + B_j - T_j)^2 + 4k_j^d T_j}. \tag{12}$$

For physically meaningful results, we require $c_j \geq 0$ so we consider only the positive root. Since no drug is lost from the system in this model (it is either bound or unbound), at steady-state the total drug concentration should be equal to the inlet concentration, i.e. $T_j = c_j^{in}$, and thus we may use (11) and (12) to calculate the partitioning of drug between b_j and c_j prior to experimentation. Note that since these expressions rely only on the parameters k_j^d and B_j, they may be used to calculate the steady-state concentrations for any drug whose interaction with the cells is governed by nonlinear saturable binding kinetics, given that the drug is supplied as a constant source and diffusion of drug within the cell region is isotropic.

2.4.2 Predicting steady-state cell surface solute concentrations when reaction is governed by Michaelis-Menten kinetics

Since experiments can span over many days and it is often possible to connect multiple bioreactor chambers together for high throughput testing, it would be useful to establish relationships between the inlet and cell surface concentrations in single and connected chambers so that cell surface solute concentration profiles may be predicted *a priori*. When the solute reaction is governed by M-M kinetics, the rate of metabolism is dependent on the solute concentration at the cell surface i.e. metabolism is variable unless the cell surface solute concentration is uniform. However, if the solute concentration is high enough i.e. $c_j \gg K_j^i$, then from (9) the rate of metabolism is approximately constant and is estimated as V_j^i . In this case, if we vary only the inlet concentration, c_j^{in}, then the *shape* of the cell surface solute concentration profile will stay approximately the same since the fluid dynamics are unchanged and approximately the same amount of solute is metabolised across the entire cell surface; however, the *magnitude* of the cell surface solute concentration will change according to the difference in the inlet concentration. Thus, provided that $R_j \approx \sum_{i=1}^{m} V_j^i$, if the cell surface concentration profile is known for a given c_j^{in}, we may predict the cell surface concentration profile for any c_j^{in} via the following equation:

$$c_j^*(y) \approx c_j(y) + \Delta c_j^{in}, \quad \Delta c_j^{in} = c_j^{in^*} - c_j^{in}, \tag{13}$$

where y is the axis through the centre of the cell surface from the inlet side to the outlet side of the chamber, $c_j^*(y)$ is the *unknown* concentration profile across the centre of the cell surface, $c_j(y)$ is the *known* concentration profile across the centre of the cell surface and Δc_j^{in} is the difference between the inlet concentrations for which the solute concentration profile across the centre of the cell surface is unknown and known, respectively. Note we have verified that this equation may be generalised to predict the concentration profile across the entire surface of the cells, but for simplicity we consider only the profile across the centre of the cell surface.

We can extend this idea to chambers connected in series: clearly, the solute concentration will decrease from the first to the last chamber due to metabolism so it would be useful to establish a relationship between the cell surface solute concentration profiles in the first chamber and in subsequent chambers. This would enable the prediction of the cell surface solute concentration profile in chamber n based only on knowledge of the profile in chamber 1. Similarly to (13), we have:

$$c_j^n(y) \approx c_j^1(y) + \Delta c_j^{in}, \quad \Delta c_j^{in} = c_j^{in^n} - c_j^{in^1},$$

where $c_j^n(y)$ is the *unknown* concentration profile across the centre of the cell surface in chamber n, $c_j^1(y)$ is the *known* concentration profile across the centre of the cell surface in chamber 1 and Δc_j^{in} is the difference between the *unknown* inlet concentration in chamber n and the *known* inlet concentration in chamber 1. Thus, in order to make use of this equation we need to be able to estimate $c_j^{in^n}$.

Let us first consider the flux entering and leaving chamber 1. At steady-state, the $\mathrm{mol\,s^{-1}}$ leaving the chamber must be equal to the $\mathrm{mol\,s^{-1}}$ entering the chamber minus the $\mathrm{mol\,s^{-1}}$ metabolised in the chamber, i.e.

$$\begin{aligned} \int_{A_{out}} \mathbf{n}\cdot\left(-D_j\nabla c_{out}^1 + \mathbf{u}_{out}^1 c_{out}^1\right)\, dA_{out} &= \int_{A_{in}} \mathbf{n}\cdot\left(-D_j\nabla c_{in}^1 + \mathbf{u}_{in}^1 c_{in}^1\right)\, dA_{in} \\ &- \int_{A_{cells}} \sum_{i=1}^{m} V_j^i\, dA_{cells}, \end{aligned} \tag{14}$$

where c_{out}^1 and c_{in}^1 ($\mathrm{mol\,m^{-3}}$) are the concentrations at the outlet and the inlet faces of chamber 1, respectively, and A_{out}, A_{in} and A_{cells} are the areas of the outlet face, the inlet face and the cell surface, respectively. Note that again we assume the metabolism is approximately constant and for convenience we define $\alpha = \int_{A_{cells}} \sum_{i=1}^{m} V_j^i\, dA_{cells}$.

Also at steady-state, the $\mathrm{mol\,s^{-1}}$ leaving chamber 1 must be equal to the $\mathrm{mol\,s^{-1}}$ entering chamber 2, i.e.

$$\int_{A_{out}} \mathbf{n}\cdot\left(-D_j\nabla c_{out}^1 + \mathbf{u}_{out}^1 c_{out}^1\right)\, dA_{out} = \int_{A_{in}} \mathbf{n}\cdot\left(-D_j\nabla c_{in}^2 + \mathbf{u}_{in}^2 c_{in}^2\right)\, dA_{in}, \tag{15}$$

and combining (15) with (14) gives:

$$\int_{A_{in}} \mathbf{n}\cdot\left(-D_j\nabla c_{in}^2 + \mathbf{u}_{in}^2 c_{in}^2\right)\, dA_{in} = \int_{A_{in}} \mathbf{n}\cdot\left(-D_j\nabla c_{in}^1 + \mathbf{u}_{in}^1 c_{in}^1\right)\, dA_{in} - \alpha. \tag{16}$$

We know that c^1_{in} is constant across A_{inlet} and if we also assume that c^2_{in} is constant then we have:

$$-D_j \nabla c^2_{in} = -D_j \nabla c^1_{in} = 0.$$

This means that we will neglect the diffusive flux and this assumption will always be appropriate when the system is convection-dominated. Then, from (16) we have:

$$c^2_{in} \int_{A_{in}} \mathbf{u}^2_{in} \cdot \mathbf{n}\, dA_{in} = c^1_{in} \int_{A_{in}} \mathbf{u}^1_{in} \cdot \mathbf{n}\, dA_{in} - \alpha,$$

and if we assume that the velocity profiles at the inlet to each chamber are identical then we obtain:

$$c^2_{in} \int_{A_{in}} \mathbf{u}^1_{in} \cdot \mathbf{n}\, dA_{in} = c^1_{in} \int_{A_{in}} \mathbf{u}^1_{in} \cdot \mathbf{n}\, dA_{in} - \alpha \implies c^2_{in} = c^1_{in} - \frac{\alpha}{\int_{A_{in}} \mathbf{u}^1_{in} \cdot \mathbf{n}\, dA_{in}} = c^1_{in} - \frac{\alpha}{Q},$$

where Q ($\mathrm{m}^3\ \mathrm{s}^{-1}$) is the input flow rate. Similarly, we have:

$$c^3_{in} = c^2_{in} - \frac{\alpha}{Q} = c^1_{in} - \frac{2\alpha}{Q},$$

and for n chambers we obtain:

$$c^n_{in} = c^1_{in} - \frac{(n-1)\alpha}{Q}.$$

Thus, provided that $R_j \approx \sum_{i=1}^{m} V^i_j$, the cell surface concentration profile in chamber 1 is known, the inlet concentrations are constant and the velocity profile at all inlets are the same, we may predict the cell surface concentration profile in chamber n via the following equation:

$$c^n_j(y) \approx c^1_j(y) - \frac{(n-1)\alpha}{Q}. \tag{17}$$

As before, we have verified that this equation may be generalised to predict the concentration profile across the entire surface of the cells, but for simplicity we consider only the profile across the centre of the cell surface.

2.5 Computational geometry

In order to demonstrate the utility of our model, we choose the geometry of a specific commercial perfusion cell culture system which is gaining popularity: the QV900 (Fig. 2a) manufactured by Kirkstall Ltd. (Rotherham, UK). The QV900 is a modular system comprising 6 cell culture chambers that can be connected together in any combination. This allows experiments to be performed either in parallel or in series, providing a high degree of flexibility as well as the potential to culture cells over a defined set of conditions.

Initially, a 3D representation of a single chamber (Fig. 2b) was constructed. The overall height of a single chamber ranges from $18.6\ \mathrm{mm}$ at the inlet side to $20.7\ \mathrm{mm}$ at the outlet side. The diameter of the chamber is taken to be $16.0\ \mathrm{mm}$, whilst the inner diameter of the inlet and the outlet is $1.0\ \mathrm{mm}$ and $1.8\ \mathrm{mm}$, respectively. The cells are assumed to be cultured at the base of the chamber in either a 3D region of height h_c or a monolayer.

We subsequently created a geometry to represent 6 chambers connected in series. Each chamber is connected by a cylindrical tube of length $100\ \mathrm{mm}$ and diameter $2.4\ \mathrm{mm}$. This is representative of a typical connecting tube, although it is noted that there is a choice of various tube lengths; however, we have verified that this feature does not significantly influence the results since employing various tube lengths from $5-100\ \mathrm{mm}$ alters the results by approximately 1% or less.

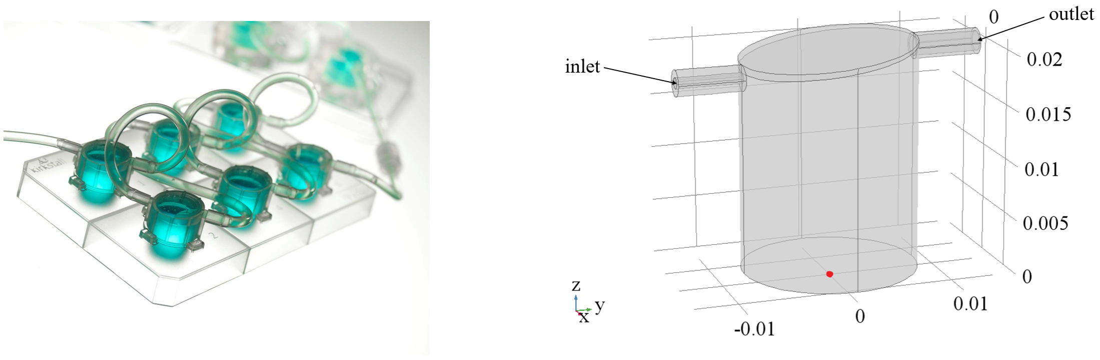

(a) (b)

Figure 2: (a) The QV900. [www.kirkstall.org] (b) Idealised 3D geometry of a single QV900 chamber, showing the orientation of the x, y and z axes where the origin is located at the centre of the base (indicated by the red dot). Note that length scales are in m.

2.6 Parameter values

There are a number of parameters in the model that can be adjusted to represent different cell culture conditions. Variable parameters such as input flow rate and inlet concentration are specified for each set of results and Table 1 presents the remaining parameters. For simplicity, the values of ρ and μ are chosen under the assumption that the fluid is water; however, it is recognised that these parameters may vary depending on the specific fluid used. Also note that for this study we assume isotropic diffusion of solute within the 3D cell region and choose $D_j^{cell} = D_j$, but we acknowledge that in reality these parameters may differ. To illustrate the results of our model, we choose representative parameters for three different solutes. For the reaction governed by nonlinear saturable binding, we describe the action of sirolimus (a drug with potent anti-proliferative and immunosuppressive properties commonly used to coat arterial stents) on smooth muscle cells. For the reaction goverened by M-M kinetics, we describe O_2 consumption for four different cell types (rat cardiomyocytes, human cardiomyocytes, rat hepatocytes and HepG2 cells) and we describe APAP metabolism using parameters obtained from a study performed *in vivo* in humans. Note that the maximum reaction rate for M-M kinetics is often provided in varying units for different solutes; in order to balance the equations we need to either multiply this parameter by the cell density or divide this parameter by the cell area for O_2 and APAP, respectively.

Parameter description	**Value**	**Reference**
Fluid parameters:		
Density (ρ)	9.94×10^2 kg m^{-3}	[17]
Dynamic viscosity (μ)	6.89×10^{-4} Pa s	[17]
Diffusion coefficients:		
Sirolimus (D_S)	2.50×10^{-10} m^2 s^{-1}	[18]
O$_2$ (D_{O_2})	3.00×10^{-9} m^2 s^{-1}	[9]
APAP (D_{APAP})	6.00×10^{-10} m^2 s^{-1}	[19]
Binding parameters for sirolimus:		
Forward reaction rate (k_f)	2.00 mol^{-1} m^3 s^{-1}	[18]
Reverse reaction rate (k_r)	5.20×10^{-3} s^{-1}	[18]
Local density of binding sites (B)	3.63×10^{-1} mol m^{-3}	[18]
Michaelis-Menten constants:		
O$_2$ (K_{O_2})	6.60×10^{-4} mol m^{-3}	[9]
Glucuronidation (K^1_{APAP})	6.89 mol m^{-3}	[14]
Sulphation (K^2_{APAP})	9.70×10^{-2} mol m^{-3}	[14]
Oxidation (K^3_{APAP})	3.03×10^{-1} mol m^{-3}	[14]
Maximum $\mathbf{O_2}$ consumption rates:		
Rat cardiomyocytes (V_{O_2})	4.01×10^{-8} mol m^{-2} s^{-1}	[20]
Human cardiomyocytes (V_{O_2})	9.81×10^{-8} mol m^{-2} s^{-1}	[20]
Rat hepatocytes (V_{O_2})	2.39×10^{-8} mol m^{-2} s^{-1}	[21]
HepG2 cells (V_{O_2})	1.17×10^{-8} mol m^{-2} s^{-1}	[21]
Maximum APAP metabolic rates:		
Glucuronidation (V^1_{APAP})	8.86×10^{-2} mol m^{-2} s^{-1}	[14]
Sulphation (V^2_{APAP})	1.02×10^{-3} mol m^{-2} s^{-1}	[14]
Oxidation (V^3_{APAP})	3.41×10^{-4} mol m^{-2} s^{-1}	[14]
General parameters:		
Total number of cells (N)	1.00×10^5 cell	this study
Volume of a smooth muscle cell (V_{cell})	1.50×10^{-14} m^3	[22]
Area covered by the cells (A)	2.01×10^{-4} m^2	this study
Thickness of 3D cell region ($h_c = NV_{cell}/A$)	7.46×10^{-6} m	this study
Cell density ($d = N/A$)	4.97×10^8 cell m^{-2}	this study

Table 1: Parameter values.

2.7 Numerical implementation

Since the equations describing fluid flow are independent of solute concentration, we first solved the fluid equations and then used this solution to subsequently solve the transport equations. The computational geometry was constructed and the finite element method was implemented in COMSOL Multiphysics. Since preliminary simulations showed that the solution to the problem is symmetric about the y, z plane passing through the origin, we used symmetry of the geometry to reduce the computational cost of the model so that only half of the problem was solved numerically. The computational mesh was generated using the physics-controlled 'Extremely fine' setting. The final mesh consisted of $2,152,947$ elements with size ranging from 0.03 to 0.46 mm and, where we modelled the cells as a 3D region, we generated a swept triangular mesh in this domain. Note that we consider only the steady-state results since we assume equilibrium is established relatively quickly, but the model may be used to generate time-dependent solutions if required.

3 Results

3.1 Fluid dynamics

We describe the velocity profile and cell surface shear stress in a single chamber for $Q = 100 - 1000\ \mu\mathrm{L\ min}^{-1}$, covering a realistic range of operating flow rates. As an example, we display only the results for $Q = 100\ \mu\mathrm{L\ min}^{-1}$ (Fig. 3) and the corresponding results for the remaining flow rates can be found in the Supplementary Material. In this case, some small zones of recirculation arise around the periphery at the base of the chamber and the peak flow speed ($4.20 \times 10^{-3}\ \mathrm{m\ s}^{-1}$) is located at the inlet. Given the considerable decrease in flow speed with chamber depth, in Fig. 3b we use a log scale to plot the velocity magnitude in order to better emphasise the variation in flow speed throughout the chamber. The magnitude of the cell surface shear stress is of the order of $10^{-8}\ \mathrm{Pa}$ and the shear stress profile displays symmetry, rising from all sides of the chamber towards the peak ($6.39 \times 10^{-8}\ \mathrm{Pa}$) located at the centre. As input flow rate is increased, the recirculation zones increase in size and eventually merge to form one large zone which takes up the majority of the chamber. The cell surface shear stress rises in magnitude with increasing input flow rate and the symmetric profile changes most substantially between $Q = 200\ \mu\mathrm{L\ min}^{-1}$ and $Q = 500\ \mu\mathrm{L\ min}^{-1}$, where the flow pattern transforms dramatically. We note that for chambers connected in series there is no significant difference in the fluid dynamics in downstream chambers (not shown).

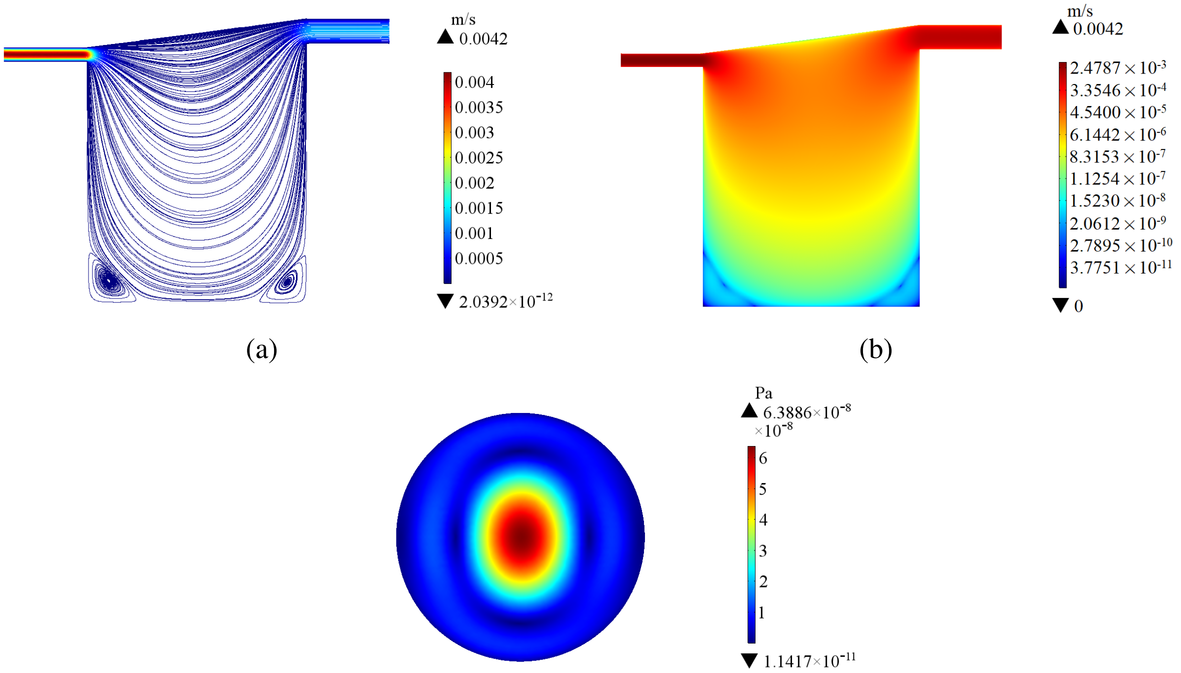

(a)

(b)

(c)

Figure 3: Simulation results for $Q = 100\ \mu\mathrm{L\ min}^{-1}$. (a) Streamlines and magnitude of velocity through the centre of the chamber on the y, z plane. (b) Magnitude of velocity through the centre of the chamber on the y, z plane using a log scale. (c) Magnitude of shear stress at the cell surface on the x, y plane.

The peak cell surface flow speed and shear stress increase with input flow rate in a nonlinear manner (Fig. 4). As input flow rate increases, the peak cell surface flow speed and shear stress increase until around $Q = 300\ \mu\mathrm{L\ min}^{-1}$ where the profiles dip. After $Q = 400\ \mu\mathrm{L\ min}^{-1}$ the peak cell surface flow speed and shear stress increase rapidly with increasing input flow rate. We deduced that a significant change in the pattern of flow is responsible for the dip: up to $Q = 200\ \mu\mathrm{L\ min}^{-1}$ and after $Q = 500\ \mu\mathrm{L\ min}^{-1}$ the behaviour of the flow is relatively unchanging, whereas in between we observe substantial differences in the appearance of the streamlines (most noticeably in the merging of the recirculation zones) and cell surface shear stress profiles (see Supplementary Material).

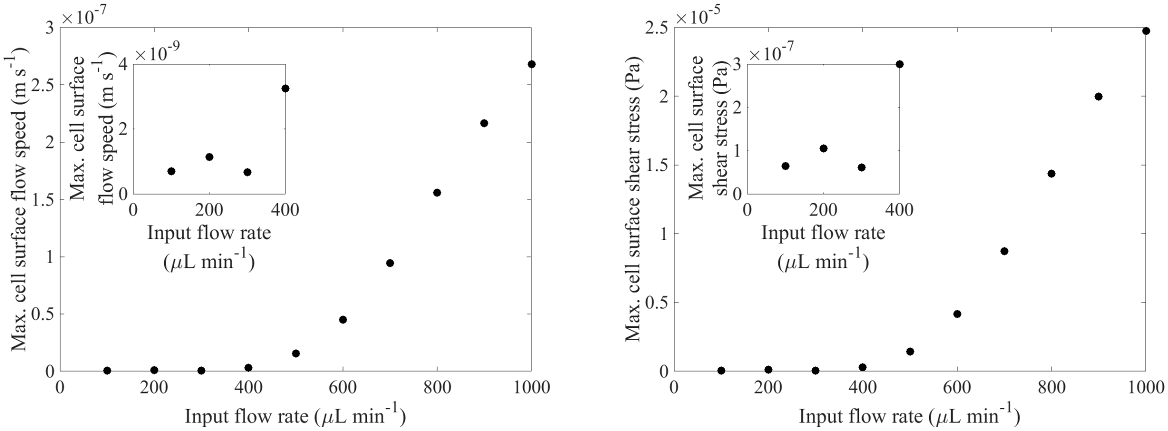

(a) (b)

Figure 4: Relationship between input flow rate and peak cell surface flow speed (a) and shear stress (b) with the inset plots illustrating each relationship up to $Q = 400\ \mu\mathrm{L\ min}^{-1}$. Note that since the velocity is equal to zero on the cell surface, we evaluate the 'cell surface' flow speed just above the cell surface.

3.2 Reaction governed by nonlinear saturable binding kinetics

We examine drug concentration profiles in the chamber for an input flow rate of $Q = 100\ \mu\mathrm{L\ min}^{-1}$ and a nominal inlet sirolimus concentration of $c_S^{in} = 5.00 \times 10^{-3}\ \mathrm{mol\ m}^{-3}$. Our simulations confirm (not shown) that at steady-state the concentration profiles are uniform in the chamber and within the cell layer, in line with our rationale described in Section 2.4.1. The significance of this result is that since the steady-state concentration profiles are uniform throughout, this implies the binding model is effectively a 1D problem which suggests the geometry of the chamber and the flow profile within the chamber are irrelevant features. To confirm this, we compared results between identical simulations using: (i) the QV900 geometry versus a simple cylindrical geometry, and (ii) flow versus no flow. The results were identical (data not shown).

3.3 Reaction governed by Michaelis-Menten kinetics

We examine solute concentration profiles in the chamber and at the cell surface for an input flow rate of $Q = 100\ \mu\mathrm{L\ min}^{-1}$. For the O_2 profiles (Fig. 5), we show results for rat cardiomyocytes as an example and we set $c_{O_2}^{in} = 0.21\ \mathrm{mol\ m}^{-3}$ to represent atmospheric O_2 levels [9]. Corresponding results for the remaining cell types are detailed in the Supplementary Material.

The $\mathrm{O_2}$ concentration decreases from $c^{in}_{O_2} = 0.21\ \mathrm{mol\ m^{-3}}$ at the top of the chamber to approximately $0.07\ \mathrm{mol\ m^{-3}}$ at the base of the chamber. The cell surface $\mathrm{O_2}$ concentration ranges from approximately 0.07 to $0.09\ \mathrm{mol\ m^{-3}}$.

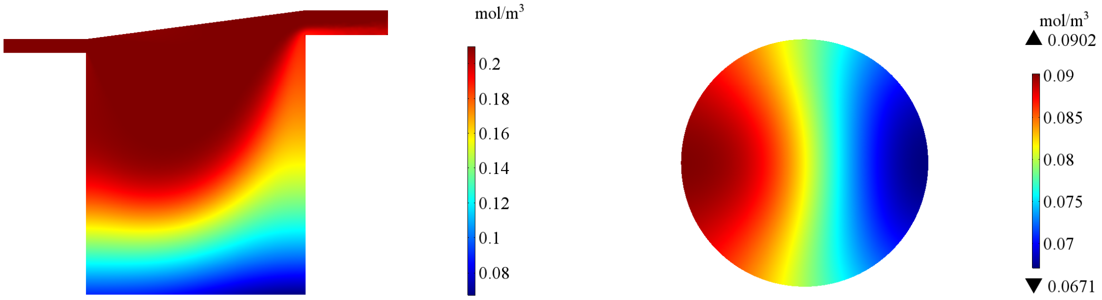

(a) (b)

Figure 5: Simulation results for rat cardiomyocytes with $Q = 100\ \mu\mathrm{L\ min^{-1}}$ and $c^{in}_{O_2} = 0.21\ \mathrm{mol\ m^{-3}}$. (a) $\mathrm{O_2}$ concentration profile through the centre of the chamber on the y, z plane. (b) $\mathrm{O_2}$ concentration at the cell surface on the x, y plane

Similar trends are observed for the APAP profiles (Fig. 6). Here we show the results for human liver cells with an inlet concentration of $c^{in}_{APAP} = 0.4\ \mathrm{mol\ m^{-3}}$ to represent a dose of $60\ \mathrm{mg/kg}$ [14]. The APAP concentration decreases from $c^{in}_{APAP} = 0.4\ \mathrm{mol\ m^{-3}}$ at the top of the chamber to approximately $9.15 \times 10^{-7}\ \mathrm{mol\ m^{-3}}$ at the base of the chamber. The APAP concentrations are very low at the cell surface, ranging from approximately 9.15×10^{-7} to $1.86 \times 10^{-6}\ \mathrm{mol\ m^{-3}}$, suggesting that the majority of the APAP is metabolised by the cells.

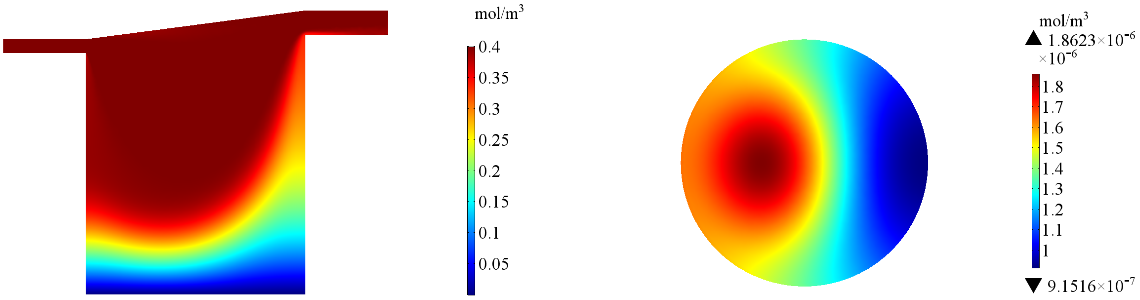

(a) (b)

Figure 6: Simulation results for human liver cells with $Q = 100\ \mu\mathrm{L\ min^{-1}}$ and $c^{in}_{APAP} = 0.4\ \mathrm{mol\ m^{-3}}$. (a) APAP concentration profile through the centre of the chamber on the y, z plane. (b) APAP concentration at the cell surface on the x, y plane

In Fig. 7 we plot the average cell surface concentration versus flow rate for both $\mathrm{O_2}$ and APAP. In the case of oxygen consumption we consider four cell types (rat cardiomyocytes, human cardiomyocytes, rat hepatocytes and HepG2 cells), whilst for APAP we consider only human liver cells due to the available data. The results of the simulations show that the average cell surface concentration tends to increase as input flow rate increases across all cell types. As with the profiles for the peak cell surface flow speed and shear stress, we observe a dip in average cell surface concentration at around $Q = 300\ \mu\mathrm{L\ min}^{-1}$ which is explained by changes in the flow pattern between $Q = 200\ \mu\mathrm{L\ min}^{-1}$ and $Q = 500\ \mu\mathrm{L\ min}^{-1}$.

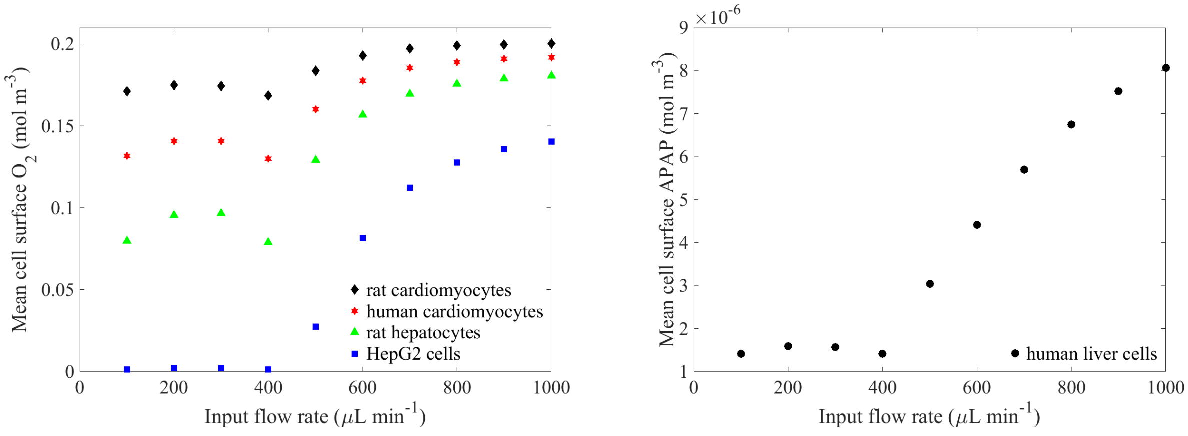

(a) (b)

Figure 7: Relationship between input flow rate and average cell surface O_2 (a) and APAP (b). These results correspond to input solute concentrations of $c^{in}_{O_2} = 0.21\ \mathrm{mol\ m}^{-3}$ and $c^{in}_{APAP} = 0.4\ \mathrm{mol\ m}^{-3}$, respectively.

Next, we test our hypotheses (13) and (17) which should allow for the prediction of the solute concentration profiles at the cell surface in single and connected chambers, respectively. Recall that these relationships inherently assume that the rate of metabolism is constant and so only hold true for $c_j \gg K^i_j$. For the parameters in Table 1, this criteria is not satisfied by APAP and so we consider O_2 as an example and illustrate the results for rat cardiomyocytes. In Fig. 8a we compare our prediction of the cell surface O_2 concentration profile from (13) to the results of the simulation when we increase the inlet concentration from $c^{in}_{O_2} = 0.21\ \mathrm{mol\ m}^{-3}$ to $c^{in}_{O_2} = 0.3\ \mathrm{mol\ m}^{-3}$, and excellent agreement is found. Integrating (13) with respect to y over the diameter of the cell surface ($-r < y < r$) gives:

$$\underbrace{\frac{\int_{-r}^{r} c^*_j(y)\, dy - \int_{-r}^{r} c_j(y)\, dy}{2r\Delta c^{in}_j}}_{\gamma_1} \approx 1. \tag{18}$$

The quantity γ_1 provides a measure of how good the approximation (13) is. Therefore, to test the validity of our hypothesis for predicting the cell surface solute concentration profile in a single chamber when the inlet concentration is varied, we evaluated (18) for $Q = 100\ \mu\mathrm{L\ min}^{-1}$ and $Q = 1000\ \mu\mathrm{L\ min}^{-1}$ with $c^{in}_{O_2} = 0.21\ \mathrm{mol\ m}^{-3}$. Fig. 8b demonstrates that $\gamma_1 \approx 1$ for the majority of these cases, with the prediction improving for higher inlet concentrations where $c_{O_2} \gg K_{O_2}$ and metabolism is therefore approximately constant. The approximation is weakest for the lowest values of $c^{in}_{O_2}$ where this criteria is not satisfied. Note that the prediction is better for the higher flow rate: increasing input flow rate gives rise to higher cell surface concentrations and so the assumption of $c_{O_2} \gg K_{O_2}$ is more accurate in this case.

In certain cases, it may be that the quantity of interest is the *mean* cell surface concentration, rather than spatial profiles. We have demonstrated that our formula (13) extends to the case of predicting mean concentrations (Fig. 8c and Fig. 8d). Moreover, we have established that there is a linear relationship between the inlet O_2 concentration and the mean cell surface O_2 concentration for the majority of inlet O_2 concentrations considered: the linear relationship breaks down when cell surface O_2 concentrations are sufficiently low that our approximation $c_{O_2} \gg K_{O_2}$ is no longer valid. We note from Fig. 8c and Fig. 8d that the approximation breaks down at higher inlet O_2 concentrations for the lower flow rate.

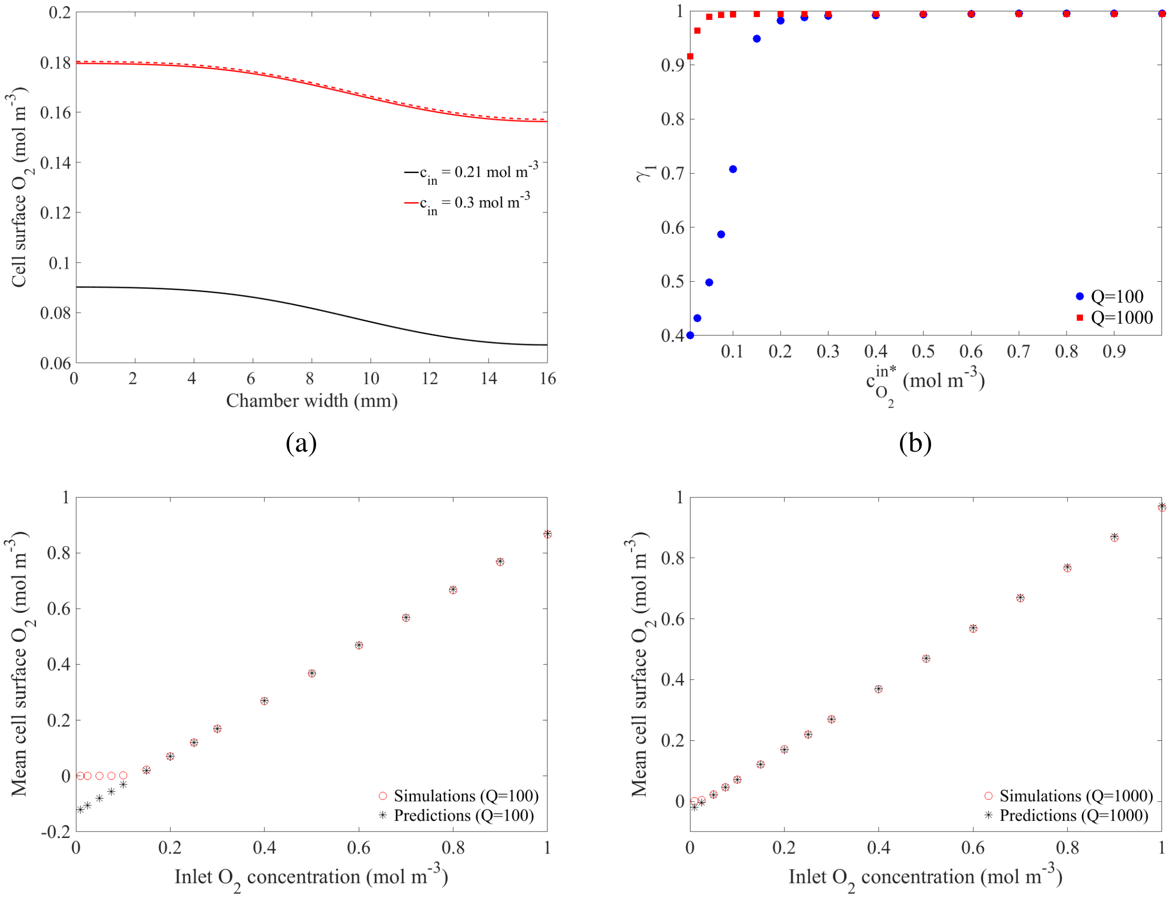

(a) (b)

(c) (d)

Figure 8: Single chamber predictions. (a) Comparison between our prediction using (13) (dashed line) and the simulation (solid line) when we increase the inlet concentration from $c^{in}_{O_2} = 0.21 \ \mathrm{mol\,m^{-3}}$ to $c^{in*}_{O_2} = 0.3 \ \mathrm{mol\,m^{-3}}$. (b) Calculated γ values for $Q = 100$ and 1000 $\mu\mathrm{L\,min^{-1}}$ with $c^{in}_{O_2} = 0.21 \ \mathrm{mol\,m^{-3}}$. (c) Relationship between inlet O_2 concentration and mean cell surface O_2 concentration for $Q = 100$ $\mu\mathrm{L\,min^{-1}}$. (c) Relationship between inlet O_2 concentration and mean cell surface O_2 concentration for $Q = 1000$ $\mu\mathrm{L\,min^{-1}}$.

To test the validity of our hypothesis for predicting the cell surface solute concentration profile in chamber n given that the profile is known in chamber 1, we first simulated the environment in chamber 1 to obtain $c^1_j(y)$ and then used (17) to predict $c^n_j(y)$ in six connected chambers for $Q = 100$ $\mu\mathrm{L\,min^{-1}}$ and $c^{in}_{O_2} = 0.21 \ \mathrm{mol\,m^{-3}}$. Fig. 9a compares the predictions (dashed lines) with the results obtained from simulations (solid lines), confirming that the predictions from (17) are in good agreement with the simulation results. As with the single chamber predictions, our formula holds also for mean cell surface concentrations (Fig. 9b) and there is a linear relationship between mean cell surface O_2 concentration and chamber number, provided that $c_{O_2} \gg K_{O_2}$.

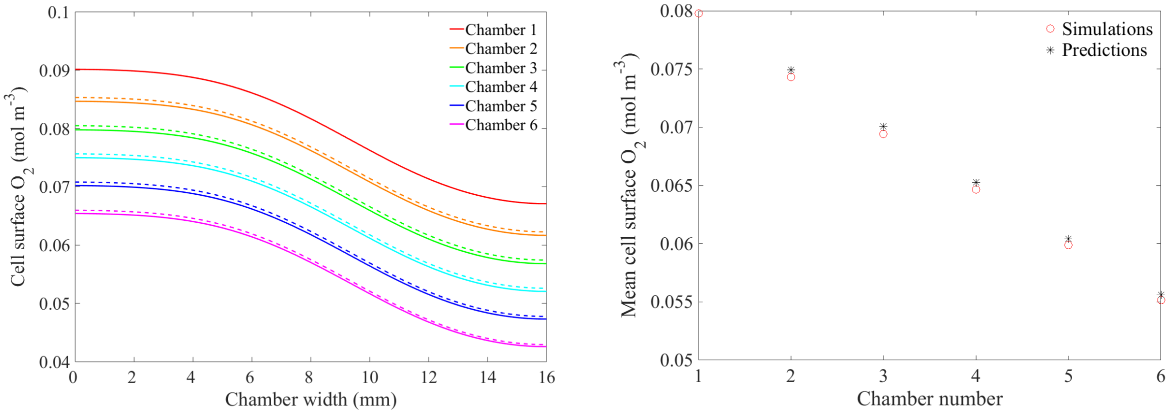

(a)

(b)

Figure 9: Connected chamber predictions for $Q = 100\ \mu\mathrm{L\ min}^{-1}$ and $c_{O_2}^{in} = 0.21\ \mathrm{mol\ m}^{-3}$. (a) Simulated (solid lines) vs. predicted (dashed lines) cell surface O_2 concentration profiles. (b) Simulated vs. predicted mean cell surface O_2 concentrations.

4 Discussion

Our findings have a number of important implications that should be considered carefully when deciding on the operating conditions of perfusion cell culture systems.

Cell surface flow speed and shear stress critically depend on the choice of input flow rate
Varying the input flow rate over a realistic range of operating flow rates gives rise to quite different fluid dynamics within the chamber and strongly influences the cell surface flow speed and shear stress levels. This means not only that the choice of flow rate is critical, but also that different flow rates should be chosen for different applications. For example, if one wishes to test the response of cells to a drug where it is known that the cells are exposed to flow *in vivo*, then the model presented here may be utilised to calculate the input flow rate that gives rise to the desired cell surface flow speed. For some applications, it may be that the cells should be exposed to slow-flow, while for other cell types it may be that high flow speeds at the cell surface are desired. Similarly, if it is known that a given cell type tolerates a known level of shear stress, then again the model may be used to select a sensible flow rate that ensures cell surface shear stress is kept within the desired range.

Spatial placement of cells influences the flow speed and shear stress that they experience
Fig. 3c shows clearly that there is a spatial distribution of shear stress at the cell surface. This means that the choice of *where* cells are placed has an impact on the level of shear stress they will experience. For example, in the case Fig. 3c, depending on the application, it may be wise not to

culture cells in the centre of the chamber, due to the peak in shear stress that occurs there. The spatial distribution of shear stress changes with flow rate (see Supplementary Material), most substantially between $Q = 200 - 500\ \mu\text{L min}^{-1}$. For flow rates outside of this range the peak is observed at the centre, whereas for flow rates within this range the pattern is not symmetric and is less predictable. Therefore, depending on the application it may well be wise to avoid these flow rates. It is also important to note that the flow speed (and consequently the magnitude of the shear stress) decreases as we move down the chamber (Fig. 3b). Therefore, one may also change the flow environment the cells are exposed to by raising the position of the cells in the chamber. The model presented here may therefore be used to optimise the spatial placement of cells within the chamber.

Flow rate and Michaelis-Menten parameters dictate cell surface solute concentrations

Fig. 7 highlights that the cell surface solute concentration is strongly influenced by both flow rate and the cell-specific M-M parameters. With the exception of the dip between $Q = 200 - 500\ \mu\text{L min}^{-1}$ (due to the change in fluid dynamics as described earlier), increasing the flow rate corresponds to increasing the solute concentration that arrives at the cell surface and is available for reaction. The variation in cell surface solute concentration across the different cell types confirms that the M-M reaction at the cell surface also has an important influence on the cell surface solute concentration. Relationships derived from the model, such as those in Fig. 7, can therefore be utilised when configuring the input flow rate for experiments in which the desired cell surface concentration is known.

Steady-state solute concentrations may be predicted a priori

In the case of reaction governed by nonlinear saturable binding kinetics, steady-state free and bound solute concentrations within the cells may be calculated *a priori* using (11-12). Since (11-12) rely only on the parameters k_j^d and B_j, they may be used to calculate the steady-state concentrations for any drug whose interaction with the cells is governed by nonlinear saturable binding kinetics, given that the drug is supplied as a constant source and diffusion of drug within the cell region is isotropic. In the case of reaction governed by M-M kinetics, we have uncovered simple relationships between inlet solute concentrations and cell surface concentration in single and connected chambers, provided that $c_j \gg K_j$ (Fig. 8 and Fig. 9). Our simple formula (13) may be used to predict changes in cell surface solute concentrations when the inlet solute concentration is altered, whilst (17) may be used to predict cell surface concentrations in downstream chambers. These relationships could be extremely useful to help determine the inlet concentration required to achieve a desired cell surface concentration, and moreover to decide on a suitable number of chambers to connect before concentrations fall below some desired level. Where possible, it is advisable to stay within the regime $c_j \gg K_j$ so that the results remain predictable.

5 Challenges

The focus of this paper has been on utilising modelling and simulation to help inform experimental operating parameters. However, these two endeavours are, of course, intrinsically linked. Mathematical and computational models require physical parameters (e.g. diffusion coefficients and metabolism rates) and these are not always known to a great degree of accuracy. It is particularly common for parameters to be gleaned from a variety of data sets, where experiments may not have been performed consistently, nor on the same type of cells or species. Sensitivity analysis may be used where there is some uncertainty over parameter values, but this has limitations, especially when the model results are highly sensitive to changes in the unknown parameters. Models, such as the one presented here, are most valuable when used in a predictive sense. However, before one may gain confidence in the model predictions, it is crucial that the model is validated. Therefore, it is critical that *in silico* tools are compared with experimental data, even if such data is limited. This can be challenging for a number of reasons. For example, it may not be easy (or possible) to take non-destructive measurements (e.g. cellular drug concentrations or O_2 concentrations at the cell surface) within certain *in vitro* perfusion systems. Advanced imaging methods can help in this regard, but these may be limited by the optical properties of the system at hand. Oxygen probes are available, but again, these cannot easily be used without disrupting the experiments. Whilst the difficulty of providing validation may be viewed as a disadvantage of modelling, it could also be seen as an advantage, i.e., modelling can allow us to obtain insight into quantities that we cannot easily measure experimentally.

The real value in modelling lies in the ability to reduce the number of experiments that have to be performed. For example, even if a system has been experimentally characterised under a given set of operating parameters, it may not be obvious how the environment changes when these operating parameters are altered. In this respect, a validated model can be invaluable, even if the validation is performed over a limited set of conditions.

The issue of model *verification* is also highly pertinent in this field, i.e., ensuring the numerical implementation of the model is correct. It is tempting to ‘believe’ results produced from computational software. However, great care must be taken to ensure the correctness and accuracy of the results. In this sense, mesh sensitivity studies and common-sense checks are both an integral part of computational modelling. However, these aspects are perhaps less familiar to non-experts, underlining the critical role of computational modellers.

These challenges only emphasise the importance of interdisciplinarity in this exciting field and that modelling and experimentation should go hand-in-hand, each complementing the other.

Acknowledgements

The authors gratefully acknowledge funding provided by EPSRC (EP/M506539/1 and EPM508056/1), a financial donation from Kirkstall Ltd. and the award of an Alan & Kathie Stross Summer Fellowship by the Dr Hadwen Trust.

References

[1] Faqi AS. A Comprehensive Guide to Toxicology In Preclinical Drug Development. Academic Press; 2012.

[2] Ng R. Drugs: From Discovery to Approval. Wiley; 2015.

[3] Hofer T, Gerner I, Gundert-Remy U, Liebsch M, Schulte A, Spielmann H, et al. Animal testing and alternative approaches for the human health risk assessment under the proposed new European chemicals regulation. Arch Toxicol. 2004;78:549–564.

[4] LeCluyse EL, Witek RP, Andersen ME, Powers MJ. Organotypic liver culture models: Meeting current challenges in toxicity testing. Crit Rev Toxicol. 2012;42:501–548.

[5] Shipley RJ, Davidson AJ, Chan K, Chaudhuri JB, Waters SL, Ellis MJ. A Strategy to Determine Operating Parameters in Tissue Engineering Hollow Fiber Bioreactors. Biotechnol Bioeng. 2011;108:1450–1461.

[6] Vozzi G, Mazzei D, Tirella A, Vozzi F, Ahluwalia A. Finite element modelling and design of a concentration gradient generating bioreactor: Application to biological pattern formation and toxicology. Toxicol In Vitro. 2010;24:1828–1837.

[7] Allen JW, Bhatia SN. Formation of Steady-State Oxygen Gradients In Vitro: Application to Liver Zonation. Biotechnol Bioeng. 2003;82:253–262.

[8] Hsu MN, Tan GS, Tania M, Birgersson E, Leo HL. Computational Fluid Model Incorporating Liver Metabolic Activities in Perfusion Bioreactor. Biotechnol Bioeng. 2014;111:885–895.

[9] Mazzei D, Guzzardi MA, Giusti S, Ahluwalia A. A Low Shear Stress Modular Bioreactor for Connected Cell Culture Under High Flow Rates. Biotechnol Bioeng. 2010;106:127–137.

[10] Mattei G, Giusti S, Ahluwalia A. Design Criteria for Generating Physiologically Relevant In Vitro Models in Bioreactors. Processes. 2014;2:548–569.

[11] Pedersen JM, Shim Y, Hans V, Phillips MB, Macdonald JM, Walker G, et al. Fluid Dynamic Modeling to Support the Development of Flow-Based Hepatocyte Culture Systems for Metabolism Studies. Front Bioeng Biotechnol. 2016;4:1–13.

[12] Pearce P, Brownbill P, Janacek J, Jirkovska M, Kubinova L, Chernyavsky IL, et al. Image-Based Modeling of Blood Flow and Oxygen Transfer in Feto-Placental Capillaries. PLOS One. 2016;11:1–22.

[13] Miners JO, Lillywhite KJ, Yoovathaworn K, Pongmarutai M, Birkett DJ. Characterization of paracetamol UDP-glucuronosyltransferase activity in human liver microsomes. Biochem Pharmacol. 1990;40:595–600.

[14] Reith D, Medlicott NJ, Silva RKD, Yang L, Hickling J, Zacharias M. Simultaneous modelling of the Michaelis-Menten kinetics of paracetamol sulphation and glucuronidation. Clin Exp Pharmacol Physiol. 2009;36:35–42.

[15] Berg JM, Tymoczko JL, Stryer L. Biochemistry. W. H. Freeman; 2002.

[16] Johnson KA, Goody RS. The Original Michaelis Constant: Translation of the 1913 Michaelis-Menten Paper. Biochemistry. 2011;50:8264–8269.

[17] Crittenden JC, Trussell RR, Hand DW, Howe KJ, Tchobanoglous G. MWH's Water Treatment: Principles and Design, Third Edition. Wiley; 2012.

[18] McGinty S, Pontrelli G. On the role of specific drug binding in modelling arterial eluting stents. J Math Chem. 2016;54:967–976.

[19] Ribeiro ACF, Barros MCF, Verissimo LMP, Santos CIAV, Cabral AMTDPV, Gaspar GD, et al. Diffusion coefficients of paracetamol in aqueous solutions. J Chem Thermodyn. 2012;54:97–99.

[20] Sekine K, Kagawa Y, Maeyama E, Ota H, Haraguchi Y, Matsuura K. Oxygen consumption of human heart cells in monolayer culture. Biochem Biophys Res Commun. 2014;452:834–839.

[21] Nyberg SL, Remmel RP, Mann HJ, Peshwa MV, Hu W, Cerra FB. Primary rat hepatocytes outperform HepG2 cells as the source of biotransformation functions in a bioartificial liver. Ann Surg. 1994;220:59–67.

[22] Milo R, Phillips R. Cell Biology by the Numbers. Garland Science; 2015.

Supplementary material for "Mathematical modelling of fluid flow and solute transport to define operating parameters for in vitro cell sulture systems"

Obtaining the parabolic inlet velocity profile from the volumetric flow rate

Here, we outline how we obtain the parabolic inlet velocity profile from the volumetric flow rate Q. Let us assume that the tube has circular cross section of radius a. Then the volumetric flow rate, Q, is given by

$$Q = 2\pi \int_0^a u(r) r dr, \tag{1}$$

where r is the distance from the inlet cylinder axis. Assuming a steady parabolic inlet velocity profile of the form $u(r) = C(a^2 - r^2)$ (C constant), then carrying out the integration in (1) and rearranging yields

$$C = \frac{2Q}{\pi a^4},$$

so that the inlet velocity profile takes the form

$$u(r) = \frac{2Q}{\pi a^4}\left(a^2 - r^2\right) = \frac{2Q}{\pi a^2}\left(1 - \frac{r^2}{a^2}\right) = 2u_0\left(1 - \frac{r^2}{a^2}\right),$$

where the parameter u_0 has units of velocity ($\mathrm{m\ s^{-1}}$).

Obtaining the reduced nonlinear saturable binding model

Here, we outline how we are able to reduce the nonlinear saturable binding model in the limit of rapid binding. Recall that for this type of reaction, within the 3D cell region we have:

$$\frac{\partial c_j}{\partial t} = D_j \nabla^2 c_j - k_j^f c_j (B_j - b_j) + k_j^r b_j, \tag{2}$$

$$\frac{\partial b_j}{\partial t} = k_j^f c_j (B_j - b_j) - k_j^r b_j. \tag{3}$$

By adding together (2) and (3) and setting $T_j = c_j + b_j$ we obtain:

$$\begin{aligned} \frac{\partial T_j}{\partial t} &= D_j \nabla^2 c_j \\ &= D_j \left(\frac{\partial^2 c_j}{\partial x^2} + \frac{\partial^2 c_j}{\partial y^2} + \frac{\partial^2 c_j}{\partial z^2}\right) \end{aligned} \tag{4}$$

$$
\begin{aligned}
&= D_j\left[\frac{\partial}{\partial x}\left(\frac{\partial c_j}{\partial x}\right)+\frac{\partial}{\partial y}\left(\frac{\partial c_j}{\partial y}\right)+\frac{\partial}{\partial z}\left(\frac{\partial c_j}{\partial z}\right)\right]\\
&= D_j\left[\frac{\partial}{\partial x}\left(\frac{dc_j}{dT_j}\frac{\partial T_j}{\partial x}\right)+\frac{\partial}{\partial y}\left(\frac{dc_j}{dT_j}\frac{\partial T_j}{\partial y}\right)+\frac{\partial}{\partial z}\left(\frac{dc_j}{dT_j}\frac{\partial T_j}{\partial z}\right)\right]\\
&= D_j\nabla\cdot\left(\frac{dc_j}{dT_j}\nabla T_j\right)\\
&= \nabla\cdot(D_j^*\nabla T_j),\quad D_j^*=D_j\frac{dc_j}{dT_j}.
\end{aligned}
$$

Assuming that binding occurs rapidly, from (3) we obtain:

$$b_j \approx \frac{B_j c_j}{k_j^d + c_j}, \tag{5}$$

where $k_j^d = k_j^r/k_j^f$ is the equilibrium dissociation constant. Substituting (5) into $T_j = c_j + b_j$ gives:

$$T_j \approx c_j + \frac{B_j c_j}{k_j^d + c_j} \implies \frac{dT_j}{dc_j} \approx 1 + \frac{B_j k_j^d}{(k_j^d + c_j)^2} \implies \frac{dc_j}{dT_j} \approx \frac{1}{1+\frac{B_j k_j^d}{(k_j^d+c_j)^2}}.$$

Results: Fluid dynamics

Figs. 1 - 9 show the velocity profile and cell surface shear stress for increasing input flow rate. For the lowest input flow rates, small zones of recirculation are observed at the periphery of the base of the chamber and the magnitude of the cell surface shear stress has a fully symmetric profile with the peak located in the centre. As input flow rate is increased, the small recirculation zones at the base of the chamber increase in size and another zone of recirculation forms just beneath the inlet. Between $Q = 300\ \mu\mathrm{L\ min}^{-1}$ and $Q = 500\ \mu\mathrm{L\ min}^{-1}$, these zones merge together to form one large recirculation zone which takes up a sizeable part of the chamber. For this range of input flow rates, the profile for the magnitude of the cell surface shear stress changes dramatically and no longer displays symmetry about the y axis. Increasing the input flow rate further sees little change in the pattern of flow; however, the magnitude of the cell surface shear stress continues to increase and symmetry about the y axis is restored with the peak once again located in the centre.

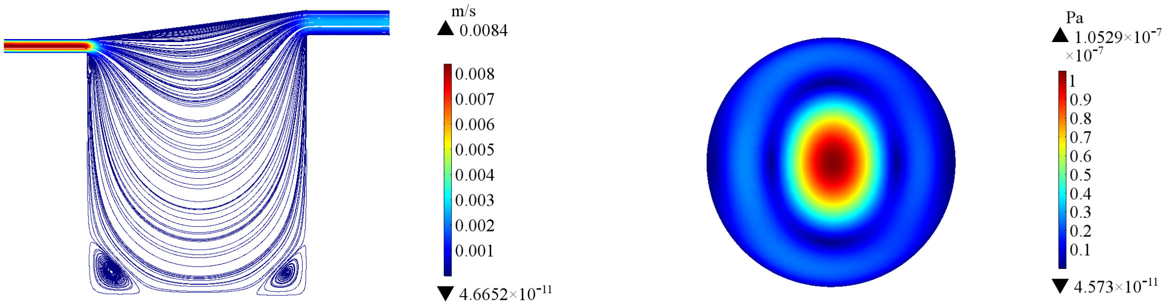

(a) (b)

Figure 1: Results for $Q = 200$ μL $\min^{-1}$. (a) Flow profile through the centre of the chamber on the y, z plane. (b) Magnitude of shear stress at the cell surface on the x, y plane.

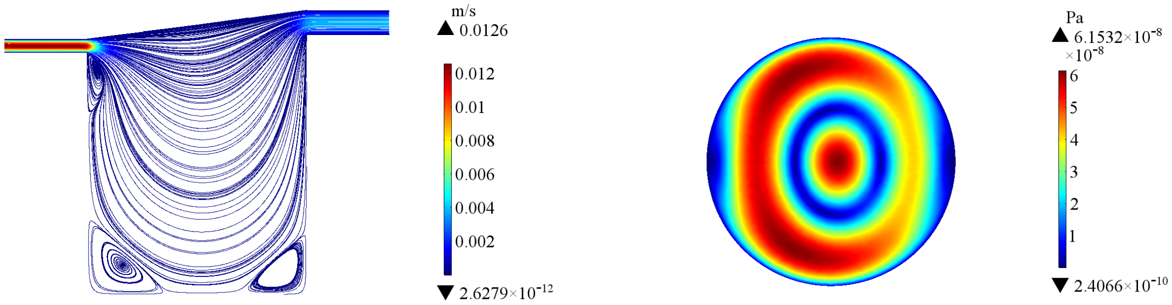

(a) (b)

Figure 2: Results for $Q = 300$ μL $\min^{-1}$. (a) Flow profile through the centre of the chamber on the y, z plane. (b) Magnitude of shear stress at the cell surface on the x, y plane.

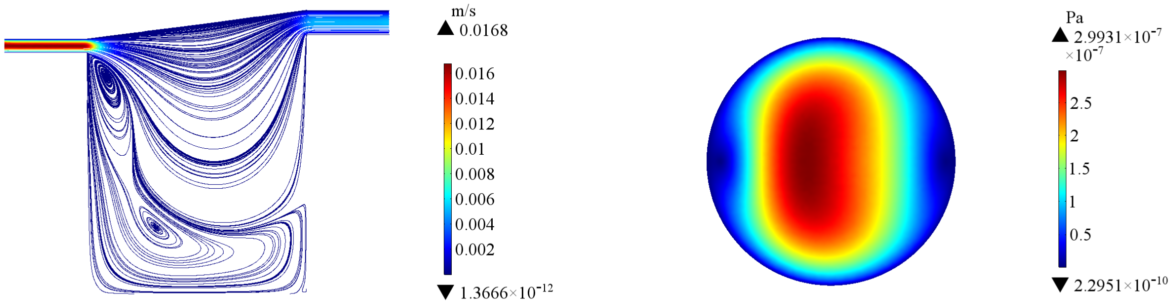

(a) (b)

Figure 3: Results for $Q = 400$ μL $\min^{-1}$. (a) Flow profile through the centre of the chamber on the y, z plane. (b) Magnitude of shear stress at the cell surface on the x, y plane.

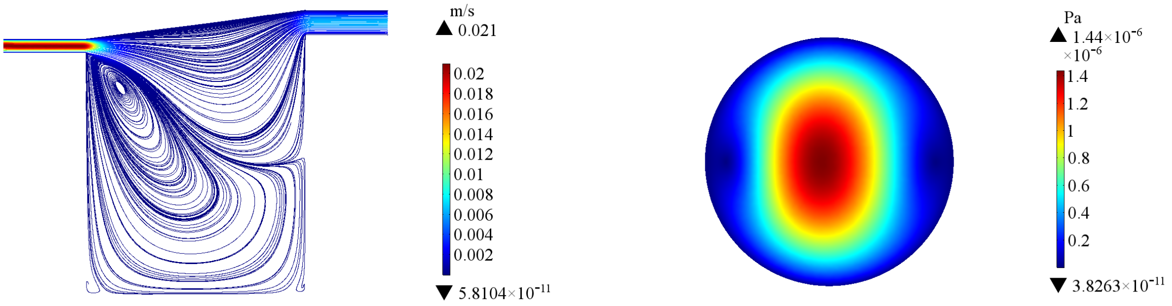

(a) (b)

Figure 4: Results for $Q = 500$ μL min^{-1}. (a) Flow profile through the centre of the chamber on the y, z plane. (b) Magnitude of shear stress at the cell surface on the x, y plane.

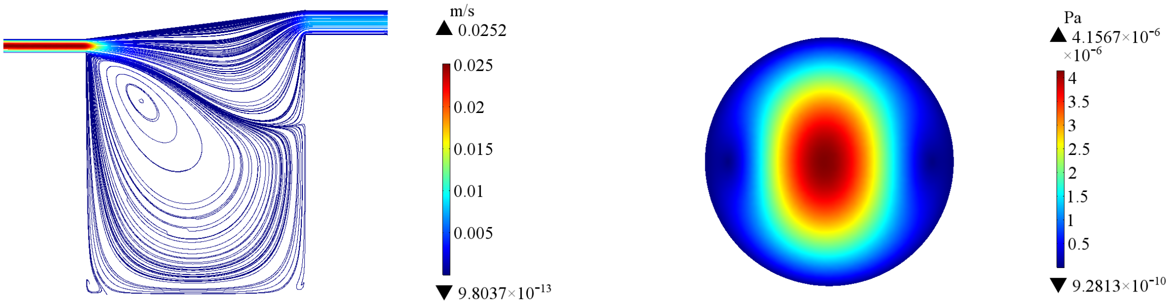

(a) (b)

Figure 5: Results for $Q = 600$ μL min^{-1}. (a) Flow profile through the centre of the chamber on the y, z plane. (b) Magnitude of shear stress at the cell surface on the x, y plane.

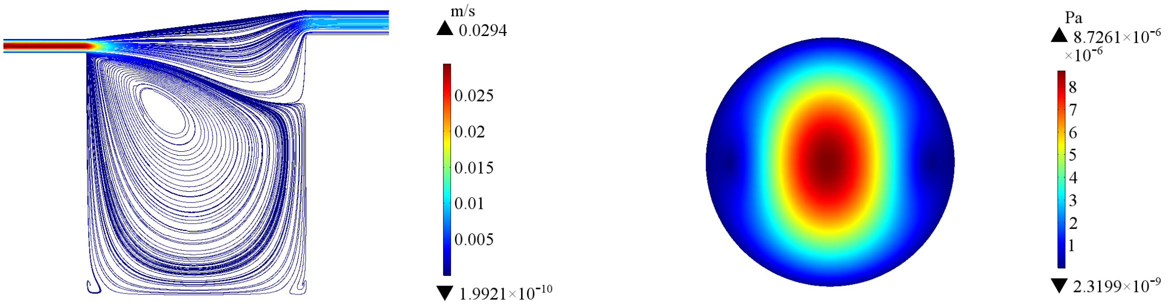

(a) (b)

Figure 6: Results for $Q = 700$ μL min^{-1}. (a) Flow profile through the centre of the chamber on the y, z plane. (b) Magnitude of shear stress at the cell surface on the x, y plane.

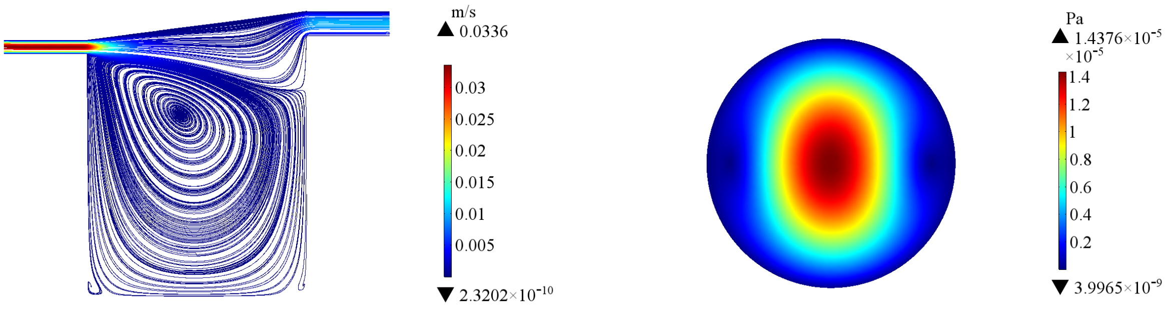

(a) (b)

Figure 7: Results for $Q = 800\ \mu\mathrm{L\ min}^{-1}$. (a) Flow profile through the centre of the chamber on the y, z plane. (b) Magnitude of shear stress at the cell surface on the x, y plane.

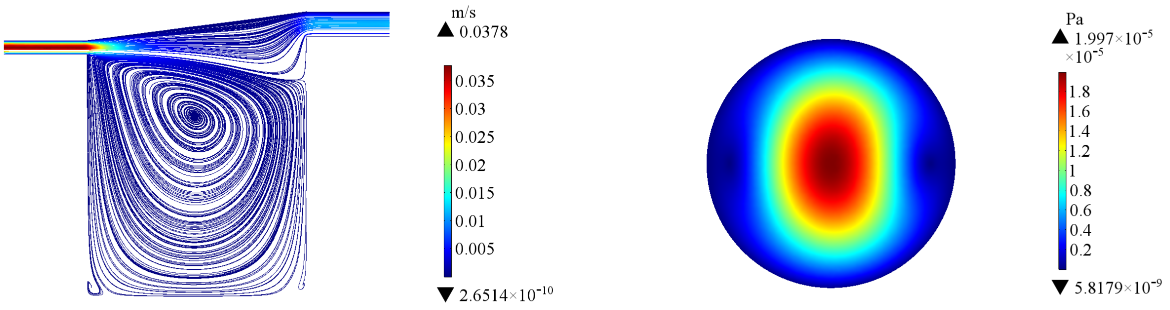

(a) (b)

Figure 8: Results for $Q = 900\ \mu\mathrm{L\ min}^{-1}$. (a) Flow profile through the centre of the chamber on the y, z plane. (b) Magnitude of shear stress at the cell surface on the x, y plane.

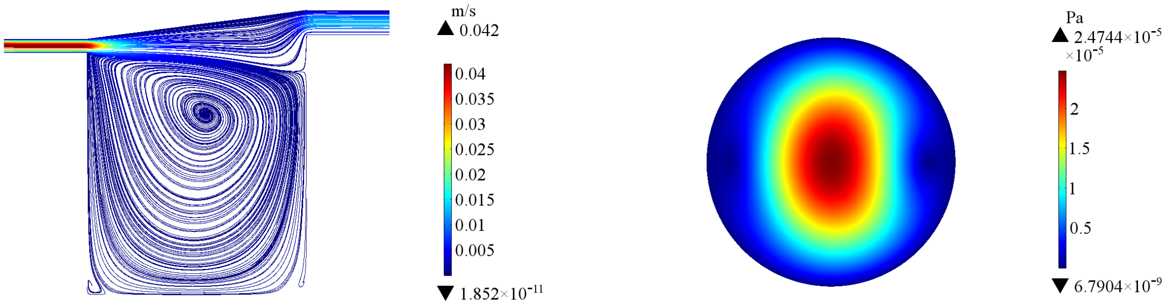

(a) (b)

Figure 9: Results for $Q = 1000\ \mu\mathrm{L\ min}^{-1}$. (a) Flow profile through the centre of the chamber on the y, z plane. (b) Magnitude of shear stress at the cell surface on the x, y plane.

Results: Reaction governed by Michaelis-Menten kinetics

Figs. 10 - 12 show the O_2 concentration profiles in the chamber and at the cell surface for various cell types with input flow rate of $Q = 100\ \mu\mathrm{L\ min}^{-1}$ and inlet concentration of $0.21\ \mathrm{mol\ m}^{-3}$. For each cell type, an O_2 concentration gradient is observed throughout the chamber. The O_2 concentration is highest (and equal to the inlet concentration) at the top of the chamber and lowest at the base of the chamber where the cells consuming O_2 are located. At the cell surface, the peak O_2 concentration is located at the inlet side of the chamber with the magnitude of the concentration varying between the cell types due to differences in the maximum O_2 consumption rates.

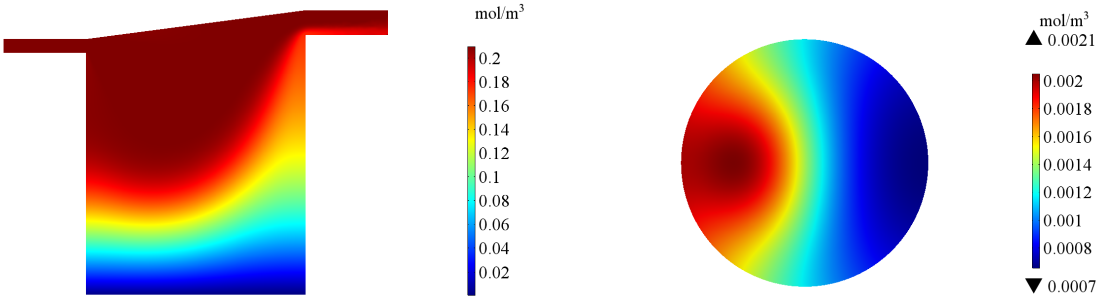

(a) (b)

Figure 10: Results for human cardiomyocytes. (a) O_2 concentration profile through the centre of the chamber on the y, z plane. (b) O_2 concentration profile at the cell surface on the x, y plane.

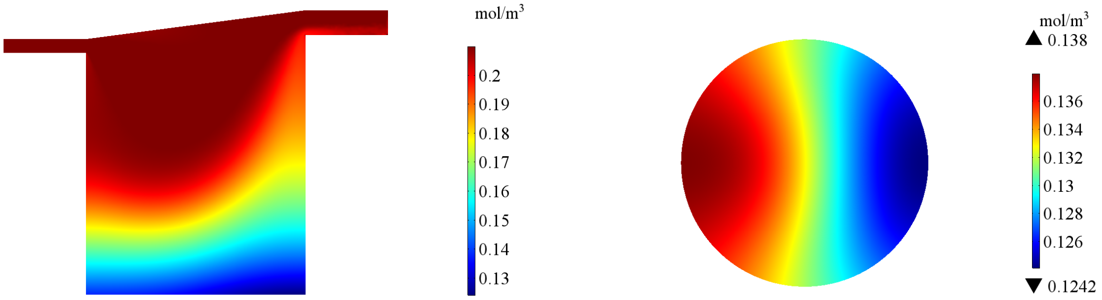

(a) (b)

Figure 11: Results for rat hepatocytes. (a) O_2 concentration profile through the centre of the chamber on the y, z plane. (b) O_2 concentration profile at the cell surface on the x, y plane.

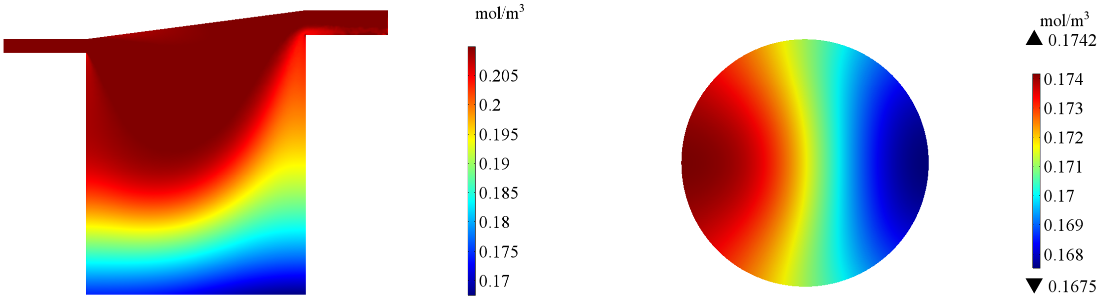

(a) (b)

Figure 12: Results for HepG2 cells. (a) O_2 concentration profile through the centre of the chamber on the y, z plane. (b) O_2 concentration profile at the cell surface on the x, y plane.